catalysts

MDPI

Article

Water-Based Electrophoretic Deposition of Ternary Cobalt-Nickel-Iron Oxides on AISI304 Stainless Steel for Oxygen Evolution

Ieva Barauskienė * and Eugenijus Valatka

Department of Physical and Inorganic Chemistry, Kaunas University of Technology, Radvilėnų Str. 19, 50254 Kaunas, Lithuania; eugenijus.valatka@ktu.lt

* Correspondence: ieva.barauskiene@ktu.lt; Tel.: +370-67622610

Abstract: Coatings consisting of cobalt, nickel and iron (Co-Ni-Fe) oxides were electrophoretically deposited on AISI 304-type stainless steel using aqueous suspensions without any binder. The synthesis of Co-Ni-Fe oxides was carried out by the thermal decomposition of metal nitrates with various molar ratios at 673 K. Structural and morphological analysis confirmed that the deposited coatings were mainly composed of spinel-type oxides with predominantly round-shaped particles. The prepared electrodes were examined for their electrocatalytic performance in oxygen generation under alkaline conditions. Various electrochemical techniques indicated the influence of iron content on the electrochemical activity of Co-Ni-Fe oxides, with the calculated values of the Tafel constant being in the range of 52–59 mV dec^{-1}. Long-term oxygen generation for 24 h at 1.0 V revealed very good mechanical and electrocatalytic stability of the prepared electrodes, since they were able to maintain up to 98% of their initial activity.

Keywords: oxygen evolution reaction; cobalt-nickel-iron oxides; thin oxide coatings; electrophoretic deposition

Citation: Barauskienė, I.; Valatka, E. Water-Based Electrophoretic Deposition of Ternary Cobalt-Nickel-Iron Oxides on AISI304 Stainless Steel for Oxygen Evolution. *Catalysts* **2022**, *12*, 490. https://doi.org/10.3390/catal12050490

Academic Editors: Sabrina Campagna Zignani and José Joaquín Linares León

Received: 29 March 2022
Accepted: 26 April 2022
Published: 28 April 2022

1. Introduction

During the last century, a steady increase in the human population has led to a rapid depletion of fossil fuel reserves and an exponential increase in carbon dioxide emissions [1]. In recent decades, advances in renewable energy technologies have decreased humanity's dependence on carbon-based energy sources. However, this progress has not been fast enough to avoid global consequences, such as a considerable rise in average global temperatures, health problems due to air pollution, and the distinction of various living species due to changing climate conditions [2,3]. In this context, hydrogen energy is considered as a great alternative to fossil fuels due to its high mass energy density and environmentally friendly combustion product: water [4]. Unfortunately, conventional hydrogen production including the steam reformation of natural gas or coal gasification discharges enormous amounts of CO_2 as a side product [5]. This circumstance hinders the wider application of hydrogen in polluted areas such as the transport sector, or in energy-intensive industrial production. Considering the zero carbon emission method for H_2 synthesis, electrochemical water splitting has become one of the most attractive ways to convert energy from renewable sources into hydrogen [6,7]. Generally, water splitting consists of water oxidation and reduction reactions, among which oxidation is considered to be more challenging as it requires the transfer of four electrons in order to form an oxygen–oxygen bond [8]. To overcome the relatively slow kinetics of oxygen evolution reaction (OER), the catalyst should meet the requirements of high efficacy, long-term stability, corrosion resistance, and low production costs [8,9]. Commercially available PEM (polymer exchange membrane) catalysis, involving both hydrogen evolution reactions (HERs) and OERs, usually employ noble electrocatalysts, such as Pt for HERs, and Ru or Ir oxides for OERs. Yet,

due to excessive price and rare abundance, these materials complicate their large-scale applications; thus, more suitable alternatives need to be developed. Our research interests are predominantly focused on the synthesis of electrocatalytic materials for alkaline-based electrolysis in the hopes of optimizing their chemical composition, stability and electroactivity. In this regard, anion exchange membrane (AEM) systems are particularly attractive due to the possibility of using earth-abundant metal electrodes, stainless steel bipolar plates, and diluted alkaline electrolytes. As it has been pointed out in [10], the successful development of AEM electrolysis technology could lead to the merging of the advantages of PEM technology (membrane separation, pure water feed) with the advantages of mature alkaline electrolysis (cheap and abundant materials). Recently, various non-precious metals and their oxides [11,12], chalcogenides [13], phosphides [14], nitrides [15], or carbides [16] have been extensively studied due to their significant activity in water splitting reactions. Still, the precise mechanism of oxygen evolution is unclear and is considered to occur on surface metal sites; therefore, the diversity of active sites is highly encouraged [17]. The introduction of more than one metal compound into the catalytic system can synergistically enhance its performance; hence, bimetallic or trimetallic structures have attracted more and more attention in recent years. Electrochemical catalysts employing transition metal-based materials, especially iron, cobalt, nickel, or molybdenum spinel-type compounds are distinguished by high catalytic efficiency, low cost, wide abundance, and excellent stability under alkaline conditions [18,19]. Recently, Qin et al. [20] synthesized a trimetallic NiFeMo alloy on nickel foam by hydrothermal deposition, which exhibited a low voltage of 1.45 V at 10 mA cm^{-2} for OER. Wu et al. [21] prepared a NiFe foam-supported $MoS_2/Fe_5Ni_4S_8$ composite for OER, which demonstrated a low overpotential of 204 mV at 10 mA cm^{-2} current density. An amorphous Ni-Fe-Mo suboxide coupled with an Ni network was obtained by Li et al. [22]. This complex was able to reach a low cell voltage of 1.50 V at 100 mA cm^{-2}. An effective and stable electrocatalyst for OER based on abundant materials could replace noble metal oxides and lift the whole process of water splitting to a higher level of large-scale application. The introduction of electrochemical techniques into the formation of thin electrocatalytic coatings is highly advantageous due to their relatively easy and accurate means of controlling the parameters, timesaving duration, suitability for mass production, and environmental friendliness, especially when alternative energy sources are used to supply the required energy [23,24]. Electrophoretic deposition (EPD) relies on the electrophoretic mobility of the particles in the solvent under the impact of the applied electric field [25]. Variations in the EPD parameters, such as applied voltage, temperature, duration, and electrolytic bath composition may easily control the weight, thickness and surface microstructure of the coatings [26]. Despite all these advantages, the exploitation of EPD usually involves volatile organic solvents such as ethanol or methanol, which must be safely disposed or recycled after use. This environmental, health and economic issue can be solved by using aqueous suspensions that additionally offer a broadened temperature range and faster kinetics during this process [25]. Water-based suspensions are still not common in electrophoresis due to the low voltage of water electrolysis and the possible bubble formation at the electrode surface. Nevertheless, our work acknowledges water to be a suitable solvent for the formation of effective and mechanically stable thin coatings.

In this work, we outline the design of a ternary electrode as a catalyst for OER by combining cobalt, nickel and iron oxides. A highly conductive, corrosion-resistant, and widely used AISI 304-type stainless steel was selected as a substrate to accelerate the electron transfer involved in OER to the external circuit [27]. Spinel-type catalysts were formed electrophoretically from aqueous suspensions without any binder. The obtained coatings were tested structurally and morphologically by various instrumental techniques. Electrochemical measurements revealed that the synthesized catalysts are promising candidates to replace noble metal compounds in OER, demonstrating good efficacy, improved kinetics, and long-term stability.

2. Results and Discussion

2.1. Electrochemical Characterization of Aqueous Suspensions of Co-Ni-Fe Oxides

The main driving force in electrophoretic deposition is the charge of the particles and their electrophoretic mobility in suspension under the influence of a particular electric field [25]. Additionally, the electric conductivity of suspension plays an important role as well. It is well established that if the suspension is too conductive then particle movement is very low and, on the contrary, if the suspension is too resistive, then the particles charge electronically and lose their stability [25]. Therefore, the mentioned parameters should be considered in order to determine the optimal conditions for the synthesis. Usually, electrophoretic deposition relies on highly volatile organic solvents such as ethanol, methanol or propanol; however, the introduction of an aqueous system implies the advantages of higher temperature control or faster kinetics, as well as the environmental, health and cost benefits which are crucial in the present day [25].

The measurements of zeta potential and other electric parameters were performed for the evaluation of the stability and surface charge of the Co-Ni-Fe oxide suspensions. Charged particles of the prepared aqueous suspensions were placed under a relatively high-frequency a.c. field (0.85–1.42 MHz) causing an oscillatory motion. The obtained experimental results are summarized in Table 1 and Figure 1. A density difference between particles and a solution forms an acoustic dipole, which is expressed as electrokinetic sonic amplitude (ESA) [28]. The experimentally determined ESA signals were used to calculate zeta potential values. It should be noted that the obtained values reflect the interplay of complex processes occurring on the surface of the mixed Co-Ni-Fe oxides (acid/base properties, adsorption of ions, surface composition, etc.). As it can be seen in Table 1, among all studied samples, CoNiFe-1 suspension was characterized by a slightly more alkaline pH, higher zeta potential, and more than twice higher conductivity compared to the other suspensions. Basically, two major mechanisms govern the surface charge at the interface between the solid particles and the aqueous solutions: (1) acid/base reactions generated by surface functional groups, and (2) the adsorption of ions [29]. Since the studied suspensions were water-based, it was presumed that $H3O^+$ and OH^- were the only ions that could be adsorbed on the surface of the oxide particle. Positive ζ values signify the dominant concentration of $H3O^+$ ions on the outside of the stationary layer. The formation of $H3O^+$ ions is a consequence of the hydroxyl groups prevailing on the surface of the transition metal oxides. According to Joseph et al. [30], the interaction between Fe 3d and water O 2p states establishes a certain substrate/adsorbate bond. The presence of this bond weakens the OH bonds within the water molecule lowering the OH dissociation energy. Right after the dissociation of H_2O, the OH^- group is adsorbed at the Fe sites; meanwhile, H^+ species are adsorbed onto a nearby oxygen site. The distance between Fe cations and O anions on the Fe_3O_4 surface fits the geometry of a water molecule. Such location could be the reason of the effective dissociation. Meanwhile, the recombinative desorption of hydroxyl and hydrogen species is rather slow, and the surface coverage of Fe_3O_4 is able to reach 0.86. The adsorption of both OH^- and H^+ might be the reason for keeping the pH value of CoNiFe-1 almost neutral. According to Campbell et al. [31], water dissociation on the NiO surface occurs rapidly, producing two types of OH species: an adsorbed one, whose oxygen atom comes from an H_2O molecule and binds with a coordinatively unsaturated Ni atom, and the other OH that is composed of an H atom from the H_2O molecule and O atom already located on the NiO surface. A rapid adsorption of OH species by NiO might cause a minor increase in the concentration of H^+ in the bulk electrolyte resulting in a mildly acidic pH. The dissociation of water molecules can occur even more readily in the presence of oxygen vacancies, as was determined by Koel et al. [32]. Concerning all the discussed peculiarities, the particles of CoNiFe-1 suspension present favorable surface properties to form stable systems for electrophoretic deposition. Its ζ value exceeds $\pm$25 mV, which is a generally accepted threshold for a stable suspension [29]. Meanwhile, other samples, though producing well-dispersed suspensions, were expected to form small conglomerates

before reaching the surface of the stainless steel substrate. This behavior might result in the enhanced porosity of the deposited coatings.

Table 1. Characteristic parameters of the aqueous suspensions of Co-Ni-Fe oxides.

Sample	ESA (mPa m V^{-1})	pH	Conductivity (mA m^{-1})	Zeta Potential (mV)	Electrophoretic Mobility (m^2 V^{-1} s^{-1})
CoNiFe-1	0.09	7.13	14.4	40.6	2.95×10^{-13}
CoNiFe-2	0.04	5.99	7.7	17.0	1.43×10^{-13}
CoNiFe-3	0.02	6.03	4.0	11.0	0.90×10^{-13}
CoNiFe-4	0.035	5.68	4.4	14.0	1.17×10^{-13}

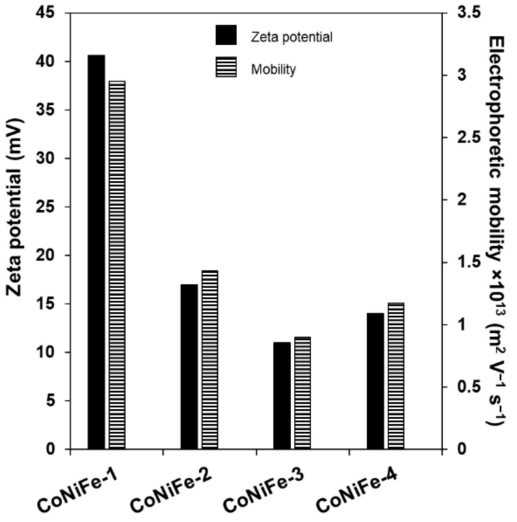

Figure 1. Variations of zeta potential and electrophoretic mobility of different Co-Ni-Fe oxide samples in water.

2.2. Structure Analysis

The structural characterization of Co-Ni-Fe oxide coatings was performed with X-ray diffraction (XRD) analysis, the results of which are displayed in Figure 2a. According to these results, two spinel-type cubic oxides, Co_3O_4 (ICDD PDF No. 80-1536, d = 0.47045, 0.28809, 0.24568, 0.23522 nm) and $NiCo_2O_4$ (ICDD PDF No. 2-1074, d = 0.28700, 0.24500, 0.20300, 0.16600 nm) were prevalent materials in all four mixes with characteristic peaks at 2θ = 18.824°, 31.044°, 36.594°, 44.471°, 55.242°, 58.956°, and 64.776°. In the case of iron oxide materials, the XRD analysis revealed certain variations between iron(II) and iron(III) oxides. Considering the CoNiFe-1 coating, where the Co, Ni and Fe molar ratio was 1:1:1, iron(III) oxide Fe_2O_3 (ICDD PDF No. 84-306, d = 0.36819, 0.26991, 0.25173, 0.22912 nm) was identified at 2θ = 24.118°, 33.136°, 35.594°, 40.912°, 49.497°, 54.090°, and 62.617°. Meanwhile, with the decreasing iron molar ratio in the synthesized samples, the presence of a cubic structured oxide Fe_3O_4 (ICDD PDF No. 26-1136, d = 0.46700, 0.28600, 0.243900, 0.23350 nm) was detected along with Fe_2O_3. However, the characterization of the CoNiFe-4 coating containing the smallest amount of iron oxide revealed peaks of only Fe_3O_4. As this form is a mix of bivalent and trivalent iron oxides, it is probable that in the presence of small quantities of Fe, cobalt and nickel parts block its full oxidation from +2 to +3. During XRD study, minor quantities of NiO (ICDD PDF No. 73-1523, d = 0.24133, 0.20900, 0.14778, 0.12603 nm) were detected in all coatings, except for CoNiFe-1. Characteristic peaks of the coatings were used for the calculations of average crystallite size according to the Scherrer equation. The obtained results given in Table 2 highlight that the composition of CoNiFe-1 could produce finer particles up to 28.1 nm. The estimation of other coating crystallite sizes

revealed that there was no significant difference in particle size on iron content, and the average size was around 37.3 ± 1 nm.

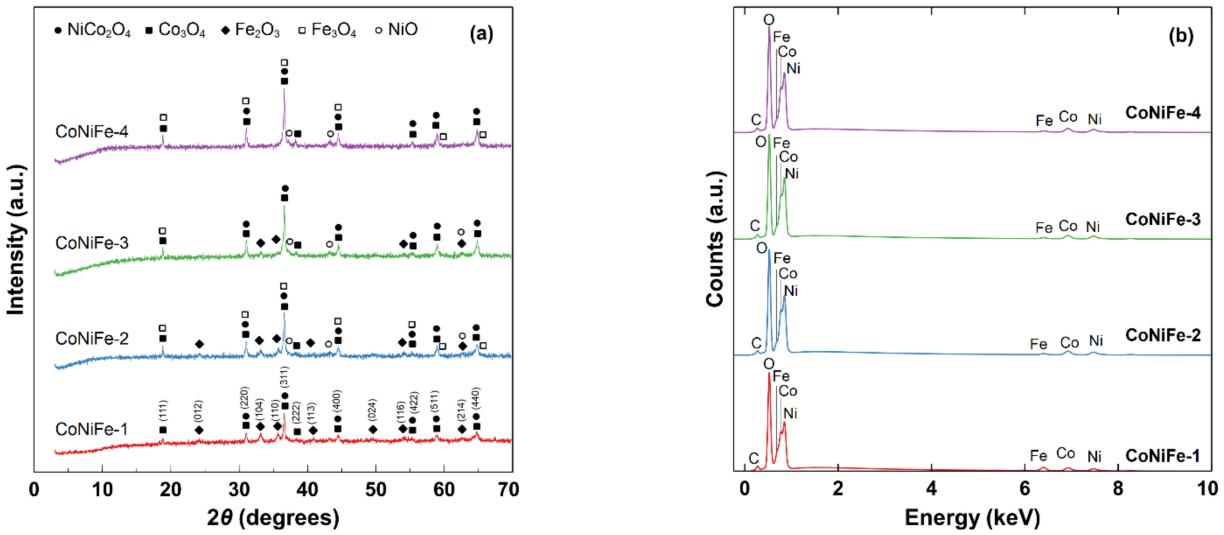

Figure 2. XRD (**a**) and EDS (**b**) patterns of Co-Ni-Fe oxides.

Table 2. Average crystallite size and composition of Co-Ni-Fe oxide samples.

Sample	Average Crystallite Size (nm)	Percentage According to XRF			Percentage According to EDS		
		Co (%)	Ni (%)	Fe (%)	Co (%)	Ni (%)	Fe (%)
CoNiFe-1	28.1	31.59	35.35	33.06	31.54	37.85	30.61
CoNiFe-2	36.7	37.26	42.35	20.39	42.73	41.88	15.39
CoNiFe-3	38.2	41.97	46.66	11.37	41.32	47.11	11.57
CoNiFe-4	37.3	42.50	49.88	4.92	43.67	47.60	8.73

The ratio between three metallic components in the prepared deposition mixes was specified with X-ray fluorescence analysis (XRF) and energy-dispersive spectroscopy (EDS). According to the results presented in Table 2, cobalt and nickel maintained the approximate ratio of 1:1 in all coatings. Meanwhile, iron content varied from 4.92 to 33.06 %, as confirmed by XRF analysis, which confirmed the calculated molar ratios in the primary prepared mixes. Meanwhile, it is clear from the EDS quantitative evaluation of coating composition that not all of the values were completely consistent with the designed CoNiFe molar ratios. For instance, the CoNiFe-4 sample showed twice higher iron content than expected. These results can be explained by the fact that EDS analysis reveals the surface composition, which can be significantly different from that of the bulk composition.

Figure 3 presents the SEM images of the electrophoretically deposited Co-Ni-Fe oxide coatings on the AISI 304 substrate. It was established that the decrease in iron content in the samples determined the apparent morphological changes. SEM micrographs confirmed that the Co-Ni-Fe samples with the lowest iron content were composed of the finest particles, evenly distributed on the surface of the stainless steel substrate (Figure 3a). The obtained results closely correlated with the regularities found during the characterization of the primary suspensions. If the charge of the particles is low, they will agglomerate even if the inter-particle distances are comparatively long, resulting in porous, sponge-like coatings [25]. The zeta potentials of CoNiFe-2, CoNiFe-3 and CoNiFe-4 did not fit into the range of a stable suspension (±25 mV), and their particles seemed to agglomerate into larger clusters before they reached the surface of the substrate. The compactness of a catalyst coating may help to overcome unwanted side processes occurring in the pores of an active material during an electrocatalytic process, e.g., OER. A catalytic reaction inside a pore is

accompanied by a diffusion of the reactants and the products. The electrolyte inside the pores is assumed to remain stagnant and the mass transport is driven by a slow molecular diffusion between the pore mouth and active centers deeper in the pore [33]. As a result, reactant concentration inside the pore is decreased, as is the reaction rate. Concerning the catalytic reaction when gaseous products are generated, its rate is determined by the pressure equilibrium between the bubbles inside the pores and the reactor. Once this is reached, the bubble is released, dragging new liquid into the pore [33,34]. This movement is chaotic and happens only near the pore mouth, leaving stagnant liquid zones in the deeper parts of the pore. Considering these obstacles, the porous structures lose their advantage of a higher surface area, and more-compact structures may turn out to be more reliable for long-term use.

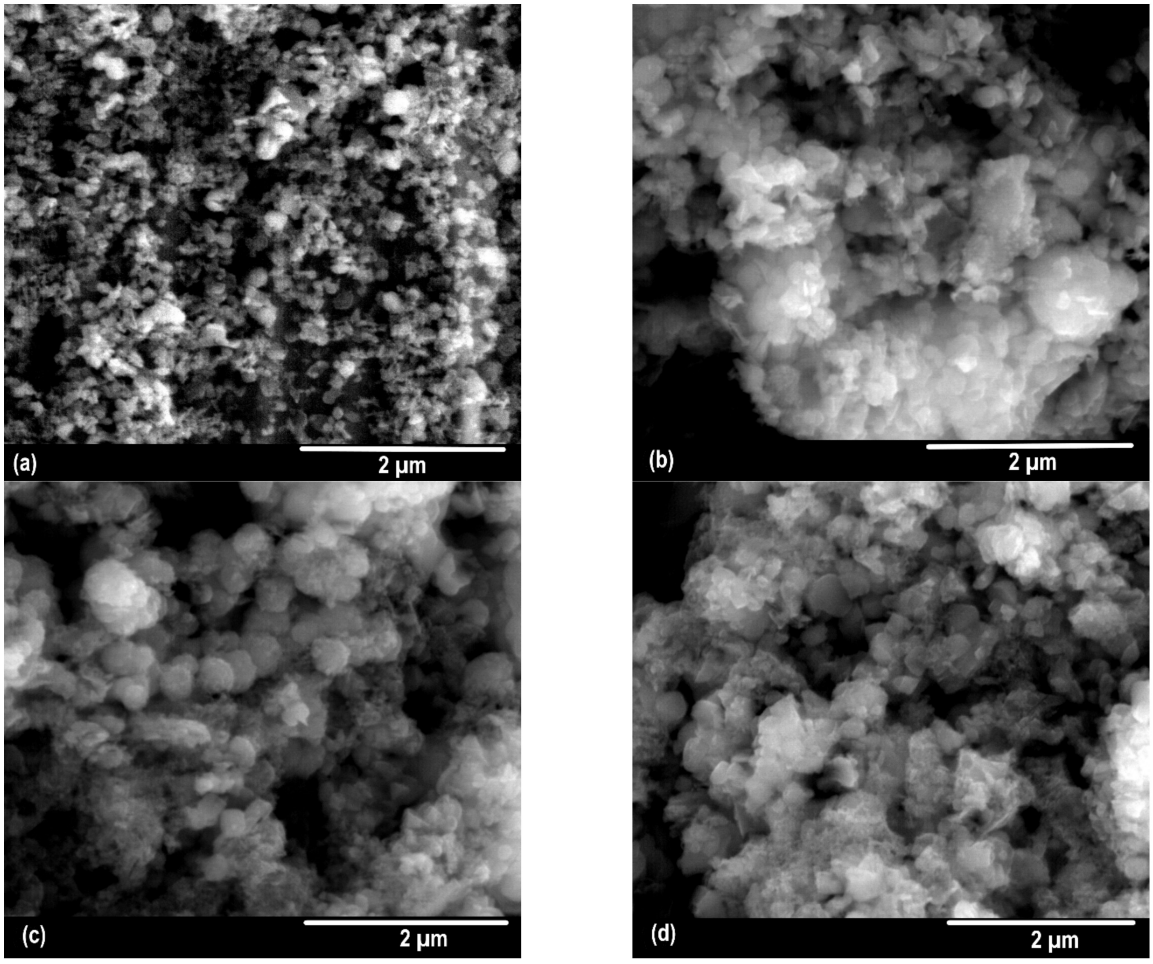

Figure 3. SEM micrographs of CoNiFe-1 (**a**), CoNiFe-2 (**b**), CoNiFe-3 (**c**), and CoNiFe-4 (**d**) at 50,000× *g* magnification.

2.3. Electrocatalytic Properties in OER

Cyclic voltammetry was applied as an initial technique for the evaluation of the electrocatalytic activity of the prepared Co-Ni-Fe coatings during the oxygen evolution reaction (OER). For this reason, the potential was swept from −1 V to +1 V at 5 mV s^{-1} scan rate in order to study the electrochemical behavior of all coatings (Figure 4a). The experimental data showed that an anodic peak in the potential range of 0.4–0.6 V was detected for all coatings. This increase in current density can be attributed to the oxidation of the $NiCo_2O_4$ and Co_3O_4 spinels, according to the following equations [35,36]:

$$NiCo_2O_4 + OH^- + H_2O \leftrightarrow NiO(OH) + CoO(OH) + e^- \quad (1)$$

$$Co_3O_4 + OH^- + H_2O \leftrightarrow 3CoO(OH) + e^- \quad (2)$$

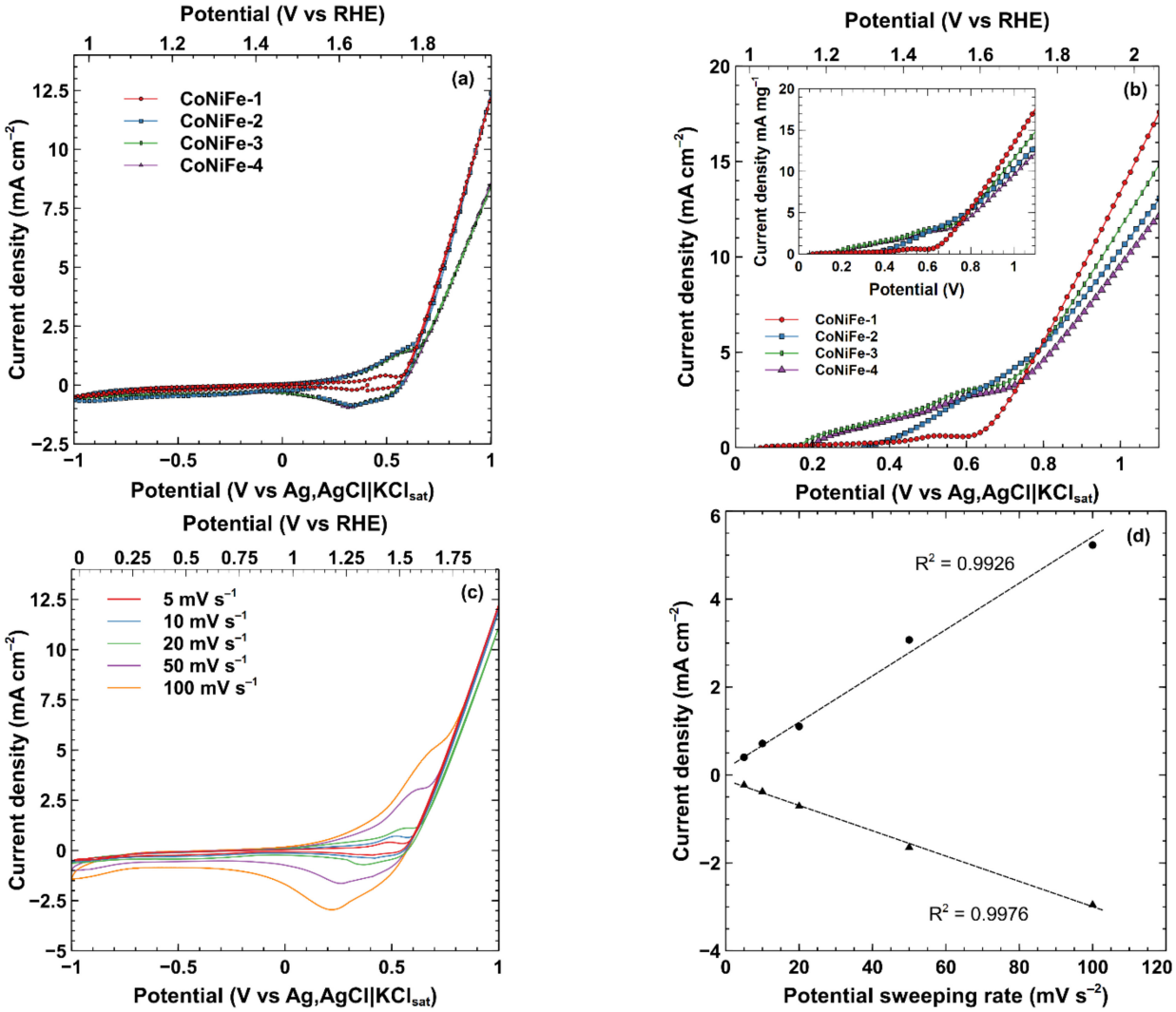

Figure 4. (**a**) Cyclic voltammograms of cobalt-nickel-iron oxides in 0.1 M NaOH at 5 mV s^{-1} potential sweeping rate. (**b**) Linear sweep voltammograms of cobalt-nickel-iron oxides in 0.1 M NaOH at 20 mV s^{-1} potential sweeping rate. Inset: linear sweep voltammograms of cobalt-nickel-iron oxides in 0.1 M NaOH normalized by mass. (**c**) Cyclic voltammograms of CoNiFe-1 sample in 0.1 M NaOH at different scan rates. (**d**) The dependency of anodic and cathodic peak (in the range of 0.2–0.6 V) currents on the potential sweep rate of CoNiFe-1 coating.

X-ray photoelectron spectroscopy (XPS) observations of the (Ni-Fe-Co-Ce)O_x system conducted by Favaro et al. [37] revealed that $Ni^{(II)}O$ and Co_3O_4 ($Co^{(II)}O{\cdot}Co^{(III)}{}_2O_3$) immediately undergo a partial conversion to $Ni^{(II)}(OH)_2$ and $Co^{(II)}(OH)_2$ at the open circuit potential when immersed. The hydroxylation of the surface is presumably initiated by the high concentration of hydroxyl ions in the electrolyte. However, X-ray adsorption spectroscopy (XAS) did not detect any signs of $Co(OH)_2$ in the bulk, suggesting that this species only forms in the outer layer of the deposited coating. Figure 4a highlights the distinctiveness of the CoNiFe-1 coating: its anodic peak is much smaller than the other coatings, with the lowest current density. Apparently, such behavior is related to the iron-rich surface. As more Fe is incorporated into the coating, it suppresses the electrochemical oxidation of $Ni^{(II)}(OH)_2$ to $Ni^{(III)}O(OH)$ [38,39]. Meanwhile, CoNiFe-2, CoNiFe-3 and CoNiFe-4 generated more intense anodic peaks in this potential range. In addition to

iron presence, the peak heights may also have been affected by the oxidation of NiO, which was identified in all coatings except for CoNiFe-1 (Figure 2) [36]:

$$NiO + OH^- \leftrightarrow NiO(OH) + e^- \quad (3)$$

The influence of cobalt should be taken into account as well. The observations carried out by Bates et al. [39] disclosed that Co facilitates the oxidation of $Ni^{(II)}$ to $Ni^{(III)}$ at lower potentials. Presumably, cobalt sites act as an indirect charge donor to Ni sites via the bridging oxygen atoms. The reversible reactions, i.e., the reduction of $Co^{(III)}$ to $Co^{(II)}$ and of $Ni^{(III)}$ to $Ni^{(II)}$, occur at around 0.3 V. Further potential sweeps to the anodic area initiate oxygen evolution.

Various approaches have been proposed to understand which elements generate active sites in complex oxide systems for electrocatalytic oxygen evolution. Still, there is no agreement on the particular mechanism of oxygen formation on the surface of transition metal oxides. Some reports state that Ni^{3+} is the active site in mixed Ni and Fe oxides [40]. A variety of cobalt oxidation states ($Co^{(II)}$, $Co^{(III)}$ and $Co^{(IV)}$) have also been suggested to be the main driving forces for OER by other authors [41,42]. Recent DFT calculations, along with XAS analysis by Bell et al. [43], have indicated that $Fe^{(III)}$ is the active site in (Ni,Fe)OOH. Some groups have proposed oxygen vacancies as the active sites due to their ability to lower the adsorption energy of the water molecules and enhance surface conductivity by creating delocalized electrons [44]. Despite the contradictions among the proposed mechanisms, the synergistic effect between nickel, cobalt and iron is evident. The presence of Co facilitates the formation of a more conductive NiO(OH) at lower potential values; thus, the activation of the $Fe^{(III)}$ sites takes place, which is otherwise inactive in the less conductive $Ni(OH)_2$ [39]. The other proposed role of Co is the contraction of the bond length Ni-O and Ni-M (M=Ni, Co, or Fe) by replacing Ni^{+2} with Co^{+3}, creating shorter bond distances because of the higher oxidation state [39]. Moreover, the addition of cobalt is presumed to induce the formation of Fe_3O_4 (where Fe is in the +2 and +3 valence states), which is more favorable for OER than monovalent Fe_2O_3.

The LSV technique was employed to take a closer look at the coatings' behavior in the anodic region where OER takes place (Figure 4b). Anodic potential sweeping showed that the highest current densities were generated by the CoNiFe-1 sample. The observed peculiarities were in agreement with the assumption that Fe^{3+} acts as the main active site for OER.

The higher activity of the CoNiFe-1 sample over other coatings may be related not only to the ratio between Co, Ni and Fe, but to its surface morphology as well. SEM micrographs disclosed a more compact morphology of the CoNiFe-1 coating (Figure 3a). As discussed previously, surface compactness and smoothness can be an advantage, helping to avoid slow process kinetics due to diffusion. To examine the impacts of diffusion and the possible hindering of the electrocatalytic surface reactions associated with it, CV scans with systematically increased scan rates were recorded. As seen in Figure 4c, the quicker scanning linearly enlarged only anodic and cathodic peak height in the potential range of 0.1–0.7 V (Figure 4d) without affecting the current density values at OER. In general, the deviation from linearity can be ascribed to inner capacitance, which is caused by the slow penetration of OH^- into less accessible areas, such as micropores, cracks, and corners, as well as slow electron transfer [45].

CV and LSV techniques have confirmed the electrocatalytic activity of ternary oxide coatings. To explore the kinetics of oxygen formation on the surface, electrochemical analysis was continued with potential controlled electrolysis in the range of 0.5–0.7 V. Each potential value was maintained for 5 min, allowing coatings to reach a steady-state potential after every measurement. Figure 5a exhibits representative current density vs. the time curves of the CoNiFe-1 coating, which demonstrated the highest OER activity during the tests. A coating's ability to maintain a steady value of current density signifies its stability during the formation of oxygen molecules. These results imply that oxide coatings composed of cobalt, nickel and iron are able to provide a balanced binding energy

of adsorbate intermediates (-OH and –O(OH)), whereas adsorbates on Ni^{+3} are bound too weakly, and Fe is known to overbind the adsorbates [43]. The construction of Tafel plots is a common method for the quantitative evaluation of OER. The plot analysis (Figure 5b) for all Co-Ni-Fe oxide coatings provided similar values of parameter *b*. Such a small *b* value as was obtained during this work (52 mV dec^{-1}) signifies good kinetic performance when process limitations are faced at the end of multiple electron transfer reactions [46]. Generally, the accepted mechanisms of oxygen evolution in transition metal oxides indicate a predominant rate-determining step when the third electron is formed in the four-electron process [47,48]:

$$M\text{-}O^* + OH^- \rightarrow M\text{-}OOH + e^- \quad (4)$$

However, it would be controversial to ascribe a particular mechanism to the Tafel slope value, since the same value can be assigned to multiple reaction mechanisms that are known to occur on the surface of transition metal oxides [49]. The observation of an abrupt change to the slope is related to the variation of active catalytic sites on applied overpotential [50]. Ni and Fe sites dominate at lower overpotentials; meanwhile, Co sites are activated at higher overpotentials.

Other authors exploring electrocatalytic systems based on cobalt, nickel and iron oxide have reported similar but slightly higher *b* values of 90 [51], 85 [52] or 68 [53] mV dec^{-1}. Although the difference is not extensive, when considering large-scale application the Co-Ni-Fe oxides synthesized in this work may arise as advantageous alternatives to iridium or ruthenium oxides.

It is clear that the Tafel analysis only permits us to estimate the parameters which reflect the apparent activity of the electrocatalytic materials (overpotential, exchange current density). It is generally accepted that the turnover frequency (TOF), defined as the ratio of product formed per unit time and the number of catalytic sites, is an accurate parameter of the intrinsic activity of a catalyst. The following equation is commonly used for the calculation of TOF [54]: $TOF = j \times N_A/(F \times n \times \Gamma)$, where j, N_A, F, n and Γ represent current density, the Avogadro constant, the Faraday constant, the number of electrons transferred to generate one molecule of a product (in a case of oxygen generation, $n = 4$), and the exact number of active sites catalyzing the reaction, respectively. In this work, however, TOF values were not estimated due to many ambiguities related to the following:

1. The lack of experimental data for the calculation of the Faradaic efficiency of the prepared electrocatalysts. The accurate quantitative measurements of the amount of oxygen evolved during OER are crucial to ensure the correctness of the calculated TOF values. In this work, the open-air electrochemical cell was employed and the amount of oxygen evolved was not experimentally determined. In many publications, one can find the estimations based on the observed current densities. However, it should be emphasized that most electrocatalytic reactions proceed through multiple steps, including continuous cycles of oxidation and the reduction of the catalyst itself [37], significantly lowering Faradaic efficiency. It is estimated [54] that, in the case of OER, the Faradaic efficiency ranges from 85 to 96% due to the fact that a considerable amount of applied charge is consumed in the self-redox reactions of the electrocatalysts;
2. The uncertainties related to the determination of the exact number of active sites. Various electrochemical methods are known to be applied for the estimation of the real surface area or the exact number of active sites, such as underpotential deposition, stripping, redox peak integration, double-layer capacitance, or redox probes. Unfortunately, these methods are very material specific, and cannot be applied universally for all types of electrocatalysts, especially multimetallic systems, as has been pointed out in critical review [54]. For example, the redox-peak integration method is applicable to only monometallic catalysts. In our opinion, the best option for the exact determination of TOF is the use of operando techniques, such as X-ray photoelectrons, X-ray absorption spectroscopies, or microscopic techniques (AFM, STM). In addition, performing experimental investigations under operando conditions elucidates the

structural changes of the electrocatalysts and the kinetic peculiarities of the OER process as a function of the applied potential [37], which cannot be obtained by using ex situ techniques.

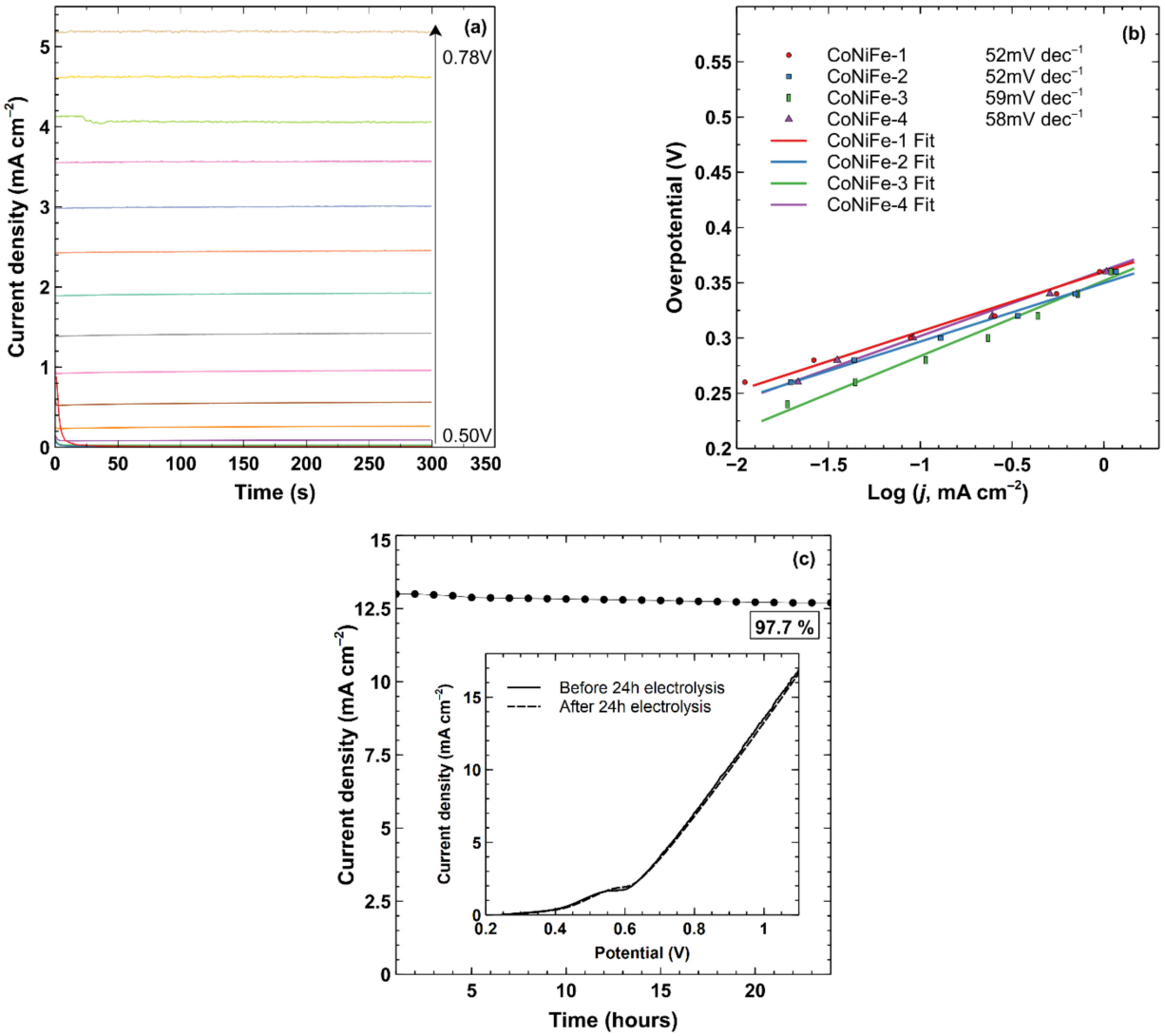

Figure 5. (**a**) Potential-controlled electrolysis of the CoNiFe-1 coating in 0.1 M NaOH. (**b**) Tafel plots of the Co-Ni-Fe oxide coatings in 0.1 M NaOH. (**c**) Long-term electrolysis results of CoNiFe-1 with LSV scans before and after (inset).

Considering the stability and durability of the electrocatalysts, several degradation processes should be assessed, such as the passivation of metallic supports, dissolution under aggressive alkaline conditions, surface deterioration during intense oxygen formation, and the peeling-off of the catalytic layer. The latter factor is especially relevant for nickel and cobalt hydroxides/oxyhydroxides because of their layered structure with large interlayer spacing. Bates et al. [39] pointed out that Ni exists in the α-Ni(OH)$_2$ or γ-NiO(OH) phase under catalytic conditions. Both of these phases exhibit interlayer spacing up to 8 Å [55]. Binninger et al. [56] proposed the idea that the stability of oxide catalysts is impossible due to the oxidation of the lattice oxygen in the bulk. Nevertheless, CoNiFe-1 coating exposed to 24-h intensive oxygen generation showed excellent catalytic performance and was able to maintain 97.7% of its initial current value (Figure 5c). Furthermore, LSV scans of pre- and post-long-term electrolysis revealed that there were no significant changes in the electrocatalytic behavior. It should be emphasized, however, that despite the fact that

the obtained characteristics of the prepared electrocatalysts were very promising, direct comparison with the testing results measured by other authors is not straightforward. In our opinion, a more systematic approach is needed for the evaluation of the performance of the prepared electrodes, for instance, an AEM electrolysis system. For this purpose, the testing of electrolyzer stacks at a laboratory scale, incorporating state-of-the-art and prepared components (commercial membrane, HER and OER electrocatalysts) is under consideration.

In order to investigate the charge transfer process of the Co-Ni-Fe oxide coatings, PEIS measurements were carried out (Table 3). The obtained results in the form of Nyquist plots along with fitted equivalent circuits are shown in Figure 6. Starting with the CoNiFe-1 coating, which previously exhibited the best electrocatalytic activity of the different coatings (Figure 6a), its equivalent circuit included a series resistance (R_s), a constant phase element describing the double-layer capacitance (CPE_{dl}), charge transfer resistance associated with Faradaic reactions on the electrolyte/electrode interface (R_{ct}), and two elements related to adsorption processes (CPE_{ads} and R_{ads}) [57]. The absence of a semicircle in the high-frequency region indicated that the rate of redox transition on the surface associated with the coating itself was very high. Meanwhile, a low-frequency semicircle was attributed to the adsorption reaction of the oxygen species [57]. Concerning the CoNiFe-2 coating, in which iron content was twice lower compared with those of cobalt and nickel, its Nyquist plot (Figure 6b) indicated a lowered semicircle diameter. This might signify some surface barriers for smooth oxygen adsorption. Besides, its equivalent circuit compatible with a plot included a constant phase element associated with a charge transfer through the Faradaic reaction CPE_{ct}. According to the XRD analysis results (Figure 2), the composition of CoNiFe-2 was the most diverse regarding the oxidation states of iron. Therefore, it is probable that various redox processes involving changes in the iron oxidation state occurred on the coating's surface. Although the double decrease in iron content exerted a considerable impact on the kinetics of the coatings' surface processes (CoNiFe-1 and CoNiFe-2), a further decrease in iron content did not demonstrate such a strong influence regarding the coatings of CoNiFe-3 (Figure 6c) and CoNiFe-4 (Figure 6d). The semicircles in the high-frequency region could be clearly observed, indicating the significance of the transitions between $Co^{(II)}/Co^{(III)}$ and $Ni^{(II)}/Ni^{(III)}$ to the whole surface charge transfers. The semicircles related to these processes were then flowed by the vertical line response. In addition to the previously named circuit elements, a modeled equivalent scheme also included a constant phase element describing the low-frequency capacitive response (CPE_c). Very similar and significantly low values of series resistance were found to be in the range of 1.2–2.2 $\Omega\ cm^{-2}$ of for all coatings.

Table 3. Characteristic parameters of aqueous suspensions of Co-Ni-Fe oxides.

Parameter	CoNiFe-1	CoNiFe-2	CoNiFe-3	CoNiFe-4
Resistance R_s ($\Omega\ cm^{-2}$)	1.16	1.82	1.37	2.23
Constant phase element CPE_{dl} ($mF{\cdot}s^{(\alpha-1)}\ cm^{-2}$)	0.248	0.151	0.982	0.238
Resistance R_{ct} ($\Omega\ cm^{-2}$)	75.6	224.2	56.0	23.9
Constant phase element CPE_{ct} ($mF{\cdot}s^{(\alpha-1)}\ cm^{-2}$)	-	3.6	19.6	8.3
Resistance R_{ads} ($\Omega\ cm^{-2}$)	459.20	4.14	0.32	8.03
Constant phase element CPE_{ads} ($mF{\cdot}s^{(\alpha-1)}\ cm^{-2}$)	0.702	2.13	0.127	0.019

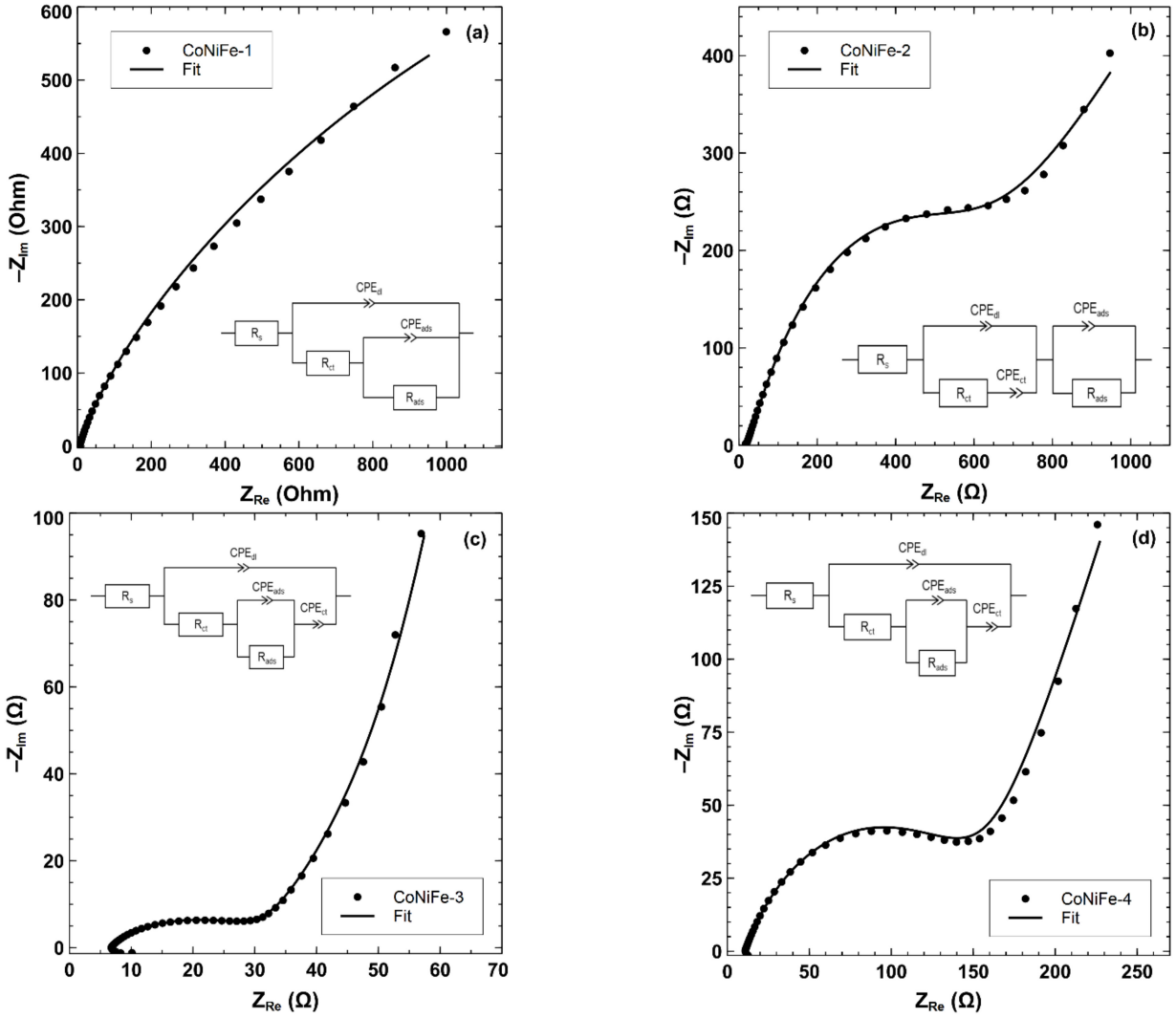

Figure 6. Nyquist plot and equivalent circuit model of cobalt, nickel and iron coatings in 0.1 M NaOH solution: (**a**) CoNiFe-1; (**b**) CoNiFe-2; (**c**) CoNiFe-3; (**d**) CoNiFe-4.

3. Materials and Methods

3.1. Synthesis of Coatings

All materials used for deposition and analysis were of analytical grade. Cobalt(II) nitrate ($Co(NO_3)_2 \cdot 6H_2O$, >99% purity, Chempur, Poland), nickel(II) nitrate ($Ni(NO_3)_2 \cdot 6H_2O$, >98% purity, Chempur, Poland), iron(III) nitrate ($Fe(NO_3)_3 \cdot 6H_2O$, >98% purity, Chempur, Poland) and sodium hydroxide (NaOH, >99% purity, Reachem, Slovakia) were used as received without further purification. The synthesis of Co-Ni-Fe oxides was carried out via thermal decomposition by mixing nitrates at various ratios and annealing at 673 K for 1 h (Table 4). According to previous experiments, these annealing conditions are favorable for the formation of electroactive spinel structures [12].

Table 4. Molar ratios of metal nitrates for the synthesis of cobalt-nickel-iron oxides.

Sample Notation	Cobalt(II) Nitrate	Nickel(II) Nitrate	Iron(III) Nitrate
CoNiFe-1	1	1	1
CoNiFe-2	1	1	0.5
CoNiFe-3	1	1	0.25
CoNiFe-4	1	1	0.1

An electrophoretic deposition (EPD) procedure was adopted for the cathodic formation of Co-Ni-Fe oxide coatings. For this purpose, 2 g of each prepared sample was dispersed in 100 mL of distilled water, stirred for 1 h at 200 rpm with a magnetic stirrer, and then treated ultrasonically for 30 min. Co-Ni-Fe oxide coatings were formed on previously cleaned AISI304 stainless steel plates (1×5 cm^2) by applying 20 V voltage. The duration of EPD in the range of 30–60 s was carefully monitored in order to form uniform and mechanically stable coatings containing the same amount of electroactive material (1.7 mg cm^{-2}). The as-prepared coatings were then dried at room temperature and annealed at 673 K for 1 h.

3.2. Structure and Morphology

The structure of the prepared Co-Ni-Fe oxide powders with various molar ratios was analyzed with X-ray diffractometer BRUKER AXS D8 operating under the following parameters: wavelength λ = 1.54056 $\times$ 10^{-10} m for Cu-Kα radiation, Ni filter, anodic voltage 40 kV, detector position step 0.02°, and current strength 40 mA. Average crystallite size (D_{hkl}) was estimated from the line broadening using the Schrerrer's equation:

$$D_{hkl} = \frac{0.94 \times \lambda}{B_{hkl} \times \cos\theta} \quad (5)$$

where λ is the wavelength of Cu-Kα radiation, B_{hkl} is the full width of the characteristic reflection peak at half maximum intensity, and θ is the Bragg diffraction angle.

The morphologies of the prepared samples were investigated by a high-resolution scanning electron microscope (Quanta FEG 200, FEI) operated at 10–20 kV. The chamber pressure was set at 80 Pa and the samples were imaged without any conductive film. An energy-dispersive X-ray spectrometer (Bruker AXS Microanalysis GmbH QUANTAX) was employed to record the element spectra.

The chemical composition analysis of Co-Ni-Fe oxide powders before the electrophoretic deposition was performed by X-ray fluorescence spectroscopy (XRF) using a Bruker X-ray S8 Tiger WD spectrometer equipped with an Rh tube with energy up to 60 keV. Measurements were conducted in a helium atmosphere and the data were analyzed with SPECTRAPlus QUANT EXPRESS standardless software.

3.3. Electrochemical Measurements

Cyclic voltammetry (CV), linear sweep voltammetry (LSV), and potentiostatic electrochemical impedance spectroscopy (PEIS) were conducted with a BioLogic SP-150 (BioLogic Science Instruments, Seyssinet-Pariset, France) potentiostat/galvanostat, employing a thermostated three-electrode cell. A platinum wire (geometric area 15 cm^2) was used as a counter electrode, Ag,AgCl | KCl$_{(sat)}$ was used as a reference electrode, and electrophoretically deposited Co-Ni-Fe oxides on AISI 304 were used as working electrodes. CV and LSV scans of all coatings for electrocatalytic activity evaluation were recorded at a potential scan rate of 5–100 mV s^{-1} in 0.1 M NaOH (stirring rate 200 rpm). EC-Lab V10.39 software was used for the collection and treatment of experimental data. Tafel plots were constructed using data of potential-controlled electrolysis in 0.1 M NaOH in an anodic potential range of 0.5–0.78 V (potential step 0.02 V). The overpotential values of η were calculated according to the following equation:

$$\eta = E_{appl} - 0.26 \quad (6)$$

where E_{appl} is applied potential in V measured against the reference electrode (Ag, AgCl | KCl$_{(sat)}$), and 0.26 is equilibrium potential against the reference electrode for water oxidation at pH 13.

Prepared aqueous suspensions for electrophoretic deposition were characterized using Field ESA zeta potential devices (PA Partikel-Analytiker-Messgeräte GmbH) in the frequency range of 0.85–1.42 MHz.

PEIS measurements were carried out in 0.1 M NaOH solution, varying the frequency range from 200 kHz to 10 mHz for open circuit potential. The sinus amplitude was 10 mV.

The pH of the solutions was measured using a Knick 766 pH meter.

All electrochemical measurements were performed at a constant temperature (293 ± 1 K).

The obtained potentials were standardized to the reversible hydrogen electrode (RHE) by the following equation and presented in the linear sweep scan results:

$$E_{RHE} = E_{Ag,AgCl} + 0.197 + 0.059 \cdot pH \quad (7)$$

4. Conclusions

Cobalt-nickel-iron oxide coatings were successfully deposited on stainless steel substrates by combining the thermal decomposition of metal nitrates and electrophoretic deposition. Environmentally friendly aqueous suspensions of various Co-Ni-Fe oxide samples were employed during electrophoretic deposition. The optimized deposition conditions permitted uniform and mechanically stable coatings containing similar amounts of electroactive materials (1.7 mg cm^{-2}). Structural analysis revealed that the coatings were predominantly composed of spinel-type cubic oxides $NiCo_2O_4$, Co_3O_4 and Fe_2O_3/Fe_3O_4. Structural, morphological and electrocatalytic properties were found to be dependent on the iron content in the prepared oxide samples. The highest electroactivity in the OERs using NaOH solutions was provided by a coating in which the Co, Ni and Fe molar ratio was 1:1:1. The synergistic effect between the metal oxides allowed us to achieve a Tafel constant as low as 52 mV dec^{-1}, clearly indicating electrocatalytic efficiency. Moreover, this sample demonstrated excellent stability after 24 h of intensive oxygen generation, maintaining 97.7 % of its primary activity. Thus, it is a very promising candidate for the replacement of noble metals and their oxides in OERs.

Author Contributions: Conceptualization, I.B. and E.V.; methodology, I.B.; software, I.B.; validation, I.B. and E.V.; formal analysis, I.B. and E.V.; investigation, I.B.; resources, I.B.; data curation, I.B.; writing—original draft preparation, I.B. and E.V.; writing—review and editing, I.B. and E.V.; visualization, I.B. All authors have read and agreed to the published version of the manuscript.

Funding: The Doctoral Fund of Kaunas University of Technology No. A-410, approved 26 June 2019.

Data Availability Statement: Not applicable.

Conflicts of Interest: The authors declare no conflict of interest.

References

1. Kment, Š.; Sivula, K.; Naldoni, A.; Sarmah, S.P.; Kmentova, H.; Kulkarni, M.; Rambabu, Y.; Schmuki, P.; Zboril, R. FeO-based nanostructures and nanohybrids for photoelectrochemical water splitting. *Prog. Mater. Sci.* **2020**, *110*, 100632. [CrossRef]
2. Das, B.; Thapper, A.; Ott, S.; Colbran, S.B. Structural features of molecular electrocatalysts in multi-electron redox processes for renewable energy–recent advances. *Sustain. Energy Fuels* **2019**, *3*, 2159–2175. [CrossRef]
3. Chu, S.; Majumdar, A. Opportunities and challenges for a sustainable energy future. *Nature* **2012**, *488*, 294–303. [CrossRef] [PubMed]
4. Turner, J.A. Sustainable hydrogen production. *Science* **2004**, *305*, 972–974. [CrossRef] [PubMed]
5. Kothari, R.; Buddhi, D.; Sawhney, R.L. Comparison of environmental and economic aspects of various hydrogen production methods. *Renew. Sustain. Energy Rev.* **2008**, *12*, 553–563. [CrossRef]
6. Roger, I.; Shipman, M.A.; Symes, M.D. Earth-abundant catalysts for electrochemical and photoelectrochemical water splitting. *Nat. Rev. Chem.* **2017**, *1*, 0003. [CrossRef]
7. Morales-Guio, C.G.; Stern, L.A.; Hu, X. Nanostructured hydrotreating catalysts for electrochemical hydrogen evolution. *Chem. Soc. Rev.* **2014**, *43*, 6555–6569. [CrossRef]
8. Deng, X.; Tuysuz, H. Cobalt-oxide-based materials as water oxidation catalyst: Recent progress and challenges. *ACS Catal.* **2014**, *4*, 3701–3714. [CrossRef]
9. Bikkarolla, S.K.; Papakonstantinou, P. $CuCo_2O_4$ nanoparticles on nitrogenated graphene as highly efficient oxygen evolution catalyst. *J. Power Sources* **2015**, *281*, 243–251. [CrossRef]
10. Miller, H.A.; Bouzek, K.; Hnat, J.; Loos, S.; Bernäcker, C.I.; Weißgärber, T.; Rontzsch, L.; Meier-Haack, J. Green hydrogen from anion exchange membrane water electrolysis: A review of recent developments in critical materials and operating conditions. *Sustain. Energy Fuels* **2020**, *4*, 2114–2133. [CrossRef]
11. Banerjee, S.; Debata, S.; Madhuri, R.; Sharma, P.K. Electrocatalytic behavior of transition metal (Ni, Fe, Cr) doped metal oxide nanocomposites for oxygen evolution reaction. *Appl. Surf. Sci.* **2018**, *449*, 660–668. [CrossRef]

12. Barauskiene, I.; Valatka, E. Layered nickel-cobalt oxide coatings on stainless steel as an electrocatalyst for oxygen evolution reaction. *Electrocatalysis* **2019**, *10*, 63–71. [CrossRef]
13. Bose, R.; Jothi, V.R.; Karuppasamy, K.; Alfantazi, A.; Yi, S.C. High performance multicomponent bifunctional catalysts for overall water splitting. *J. Mater. Chem. A* **2020**, *8*, 13795–13805. [CrossRef]
14. Sun, J.; Li, S.; Zhang, Q.; Guan, J. Iron–cobalt–nickel trimetal phosphides as high-performance electrocatalysts for overall water splitting. *Sustain. Energy Fuels* **2020**, *4*, 4531–4537. [CrossRef]
15. Wang, J.; Cao, F.; Shen, C.; Li, G.; Li, X.; Yang, X.; Li, S.; Qin, G. Nanoscale nickel–iron nitride-derived efficient electrochemical oxygen evolution catalysts. *Catal. Sci. Technol.* **2020**, *10*, 4458–4466. [CrossRef]
16. Cui, S.; Li, M.; Bo, X. Co/Mo_2C composites for efficient hydrogen and oxygen evolution reaction. *Int. J. Hydrog. Energy* **2020**, *45*, 21221–21231. [CrossRef]
17. Hu, C.; Zhang, L.; Gong, J. Recent progress made in the mechanism comprehension and design of electrocatalysts for alkaline water splitting. *Energy Environ. Sci.* **2019**, *12*, 2620–2645. [CrossRef]
18. Gu, Y.; Chen, S.; Ren, J.; Jia, Y.A.; Chen, C.; Komarneni, S.; Yang, D.; Yao, X. Electronic structure tuning in Ni_3FeN/r-GO aerogel toward bifunctional electrocatalyst for overall water splitting. *ACS Nano* **2018**, *12*, 245–253. [CrossRef]
19. Li, W.; Li, M.; Wang, C.; Wei, Y.; Lu, X. Fe doped CoO/C nanofibers towards efficient oxygen evolution reaction. *Appl. Surf. Sci.* **2020**, *506*, 144680. [CrossRef]
20. Qin, F.; Zhao, Z.; Alam, M.K.; Ni, Y.; Robles-Hernandez, F.; Yu, L.; Chen, S.; Ren, Z.; Wang, Z.; Bao, J. Trimetallic NiFeMo for overall electrochemical water splitting with a low cell voltage. *ACS Energy Lett.* **2018**, *3*, 546–554. [CrossRef]
21. Wu, Y.; Li, F.; Chen, W.; Xiang, Q.; Ma, Y.; Zhu, H.; Tao, P.; Song, C.; Shang, W.; Deng, T.; et al. Coupling interface constructions of MoS_2/$Fe_5Ni_4S_8$ heterostructures for efficient electrochemical water splitting. *Adv. Mater.* **2018**, *30*, 1803151. [CrossRef] [PubMed]
22. Li, Y.K.; Zhang, G.; Lu, W.T.; Cao, F.F. Amorphous Ni–Fe–Mo suboxides coupled with Ni network as porous nanoplate array on nickel foam: A highly efficient and durable bifunctional electrode for overall water splitting. *Adv. Sci.* **2020**, *7*, 1902034. [CrossRef] [PubMed]
23. Jiang, L.Y.; Sui, Y.W.; Qi, J.Q.; Chang, Y.; He, Y.Z.; Meng, Q.K.; Wei, F.X.; Sun, Z.; Jin, Y.X. Structure Dependence of Fe-Co Hydroxides on Fe/Co Ratio and Their Application for Supercapacitors. *Part. Part. Syst. Charact.* **2017**, *34*, 1600239. [CrossRef]
24. Wu, M.-S.; Chan, D.-S.; Lin, K.-H.; Jow, J.-J. A simple route to electrophoretic deposition of transition metal-coated nickel oxide films for electrochemical capacitors. *Mater. Chem. Phys.* **2011**, *130*, 1239–1245. [CrossRef]
25. Besra, L.; Liu, M. A review on fundamentals and applications of electrophoretic deposition (EPD). *Prog. Mater. Sci.* **2007**, *52*, 1–61. [CrossRef]
26. Wu, M.-S.; Huang, C.-Y.; Lin, K.-H. Electrophoretic deposition of nickel oxide electrode for high-rate electrochemical capacitors. *J. Power Sources* **2009**, *186*, 557–564. [CrossRef]
27. Lu, F.; Zhou, M.; Zhou, Y.X.; Zeng, X.H. First-Row Transition Metal Based Catalysts for the Oxygen Evolution Reaction under Alkaline Conditions: Basic Principles and Recent Advances. *Small* **2017**, *13*, 1701931. [CrossRef]
28. Lobbus, M.; Sonnfeld, J.; van Leeuwen, H.P.; Vogelsberger, W.; Lyklema, J. An improved method for calculating zeta-potentials from measurements of the electrokinetic sonic amplitude. *J. Colloid Interface Sci.* **2000**, *229*, 174–183. [CrossRef]
29. Luxbacher, T. *The Zeta Guide: Principles of the Streaming Potential Technique*, 1st ed.; Anton Paar GmbH: Graz, Austria, 2014.
30. Joseph, Y.; Ranke, W.; Weiss, W. Water on FeO(111) and Fe3O4(111): Adsorption behavior on different surface terminations. *J. Phys. Chem. B* **2000**, *104*, 3224–3236. [CrossRef]
31. Zhao, W.; Bajdich, M.; Carey, S.; Vojvodic, A.; Norskov, J.K.; Campbell, C.T. Water Dissociative Adsorption on NiO(111): Energetics and Structure of the Hydroxylated Surface. *Acs Catal.* **2016**, *6*, 7377–7384. [CrossRef]
32. Chen, Z.; Kronawitter, C.X.; Waluyo, I.; Koel, B.E. Investigation of Water Dissociation and Surface Hydroxyl Stability on Pure and Ni-Modified CoOOH by Ambient Pressure Photoelectron Spectroscopy. *J. Phys. Chem. B* **2018**, *122*, 810–817. [CrossRef]
33. Espinosa, R.B.; Duits, M.H.G.; Wijnperle, D.; Mugele, F.; Lefferts, L. Bubble formation in catalyst pores; curse or blessing? *React. Chem. Eng.* **2018**, *3*, 826–833. [CrossRef]
34. Datsevich, L.B. Oscillation theory: Part 4. Some dynamic peculiarities of motion in catalyst pores. *Appl. Catal. A Gen.* **2005**, *294*, 22–33. [CrossRef]
35. Si, Y.; Guo, C.; Xie, C.; Xiong, Z. An ultrasonication-assisted cobalt hydroxide composite with enhanced electrocatalytic activity toward oxygen evolution reaction. *Materials* **2018**, *11*, 1912. [CrossRef]
36. Chang, C.; Zhang, L.; Hsu, C.W.; Chuah, X.F.; Lu, S.Y. Mixed NiO/$NiCo_2O_4$ nanocrystals grown from the skeleton of a 3D porous nickel network as efficient electrocatalysts for oxygen evolution reactions. *ACS Appl. Mater. Interfaces* **2018**, *10*, 417–426. [CrossRef]
37. Favaro, M.; Drisdell, W.S.; Marcus, M.A.; Gregoire, J.M.; Crumlin, E.J.; Haber, J.A.; Yano, J. An Operando Investigation of (Ni-Fe–Co–Ce)Ox System as Highly Efficient Electrocatalyst for Oxygen Evolution Reaction. *Acs Catal.* **2017**, *7*, 1248–1258. [CrossRef]
38. Louie, M.W.; Bell, A.T. An Investigation of Thin-Film Ni–Fe Oxide Catalysts for the Electrochemical Evolution of Oxygen. *J. Am. Chem. Soc.* **2013**, *135*, 12329–12337. [CrossRef]
39. Bates, M.K.; Jia, Q.Y.; Doan, H.; Liang, W.T.; Mukerjee, S. Charge-Transfer Effects in Ni–Fe and Ni–Fe–Co Mixed-Metal Oxides for the Alkaline Oxygen Evolution Reaction. *Acs Catal.* **2016**, *6*, 155–161. [CrossRef]

40. Trzesniewski, B.J.; Diaz-Morales, O.; Vermaas, D.A.; Longo, A.; Bras, W.; Koper, M.T.M.; Smith, W.A. In Situ Observation of Active Oxygen Species in Fe-Containing Ni-Based Oxygen Evolution Catalysts: The Effect of pH on Electrochemical Activity. *J. Am. Chem. Soc.* **2015**, *137*, 15112–15121. [CrossRef]
41. Brodsky, C.N.; Hadt, R.G.; Hayes, D.; Reinhart, B.J.; Li, N.; Chen, L.X.; Nocera, D.G. In situ characterization of cofacial Co(IV) centers in Co_4O_4 cubane: Modeling the high-valent active site in oxygen-evolving catalysts. *Proc. Natl. Acad. Sci. USA* **2017**, *114*, 3855–3860. [CrossRef]
42. Tripkovic, V.; Hansen, H.A.; Vegge, T. From 3D to 2D Co and Ni Oxyhydroxide Catalysts: Elucidation of the Active Site and Influence of Doping on the Oxygen Evolution Activity. *Acs Catal.* **2017**, *7*, 8558–8571. [CrossRef]
43. Friebel, D.; Louie, M.W.; Bajdich, M.; Sanwald, K.E.; Cai, Y.; Wise, A.M.; Cheng, M.J.; Sokaras, D.; Weng, T.C.; Alonso-Mori, R.; et al. Identification of Highly Active Fe Sites in (Ni,Fe)OOH for Electrocatalytic Water Splitting. *J. Am. Chem. Soc.* **2015**, *137*, 1305–1313. [CrossRef] [PubMed]
44. Wang, J.S.; Liu, J.; Zhang, B.; Wan, H.Z.; Li, Z.S.; Ji, X.; Xu, K.; Chen, C.; Zha, D.; Miao, L.; et al. Synergistic effect of two actions sites on cobalt oxides towards electrochemical water-oxidation. *Nano Energy* **2017**, *42*, 98–105. [CrossRef]
45. Li, G.; Anderson, L.; Chen, Y.; Pan, M.; Chuang, P.-Y.A. New insights into evaluating catalyst activity and stability for oxygen evolution reactions in alkaline media. *Sustain. Energy Fuels* **2018**, *2*, 237–251. [CrossRef]
46. Suen, N.T.; Hung, S.F.; Quan, Q.; Zhang, N.; Xu, Y.J.; Chen, H.M. Electrocatalysis for the oxygen evolution reaction: Recent development and future perspectives. *Chem. Soc. Rev.* **2017**, *46*, 337–365. [CrossRef] [PubMed]
47. Zhao, Q.; Yan, Z.; Chen, C.; Chen, J. Spinels: Controlled preparation, oxygen reduction/evolution reaction application, and beyond. *Chem. Rev.* **2017**, *117*, 10121–10211. [CrossRef] [PubMed]
48. Wang, H.Y.; Hung, S.F.; Chen, H.Y.; Chan, T.S.; Chen, H.M.; Liu, B. In Operando Identification of Geometrical-Site-Dependent Water Oxidation Activity of Spinel Co_3O_4. *J. Am. Chem. Soc.* **2016**, *138*, 36–39. [CrossRef]
49. Haber, J.A.; Xiang, C.X.; Guevarra, D.; Jung, S.H.; Jin, J.; Gregoire, J.M. High-Throughput Mapping of the Electrochemical Properties of (Ni-Fe-Co-Ce)O_x Oxygen-Evolution Catalysts. *Chemelectrochem* **2014**, *1*, 524–528. [CrossRef]
50. Lindstrom, M.L.; Gakhar, R.; Raja, K.; Chidambaram, D. Facile Synthesis of an Efficient Ni–Fe–Co Based Oxygen Evolution Reaction Electrocatalyst. *J. Electrochem. Soc.* **2020**, *167*, 046507. [CrossRef]
51. Nozari-Asbemarz, M.; Amiri, M.; Khodayari, A.; Bezaatpour, A.; Nouhi, S.; Hosseini, P.; Wark, M.; Boukherroub, R.; Szunerits, S. In Situ Synthesis of $Co_3O_4/CoFe_2O_4$ Derived from a Metal—Organic Framework on Nickel Foam: High-Performance Electrocatalyst for Water Oxidation. *Acs Appl. Energy Mater.* **2021**, *4*, 2951–2959. [CrossRef]
52. Madakannu, I.; Patil, I.; Kakade, B.A.; Kasibhatta, K.R.D. Boosting oxygen evolution reaction performance by nickel substituted cobalt-iron oxide nanoparticles embedded over reduced graphene oxide. *Mater. Chem. Phys.* **2020**, *252*, 123238. [CrossRef]
53. Hao, Z.W.; Wei, P.K.; Kang, H.Z.; Yang, Y.; Li, J.; Chen, X.; Guo, D.G.; Liu, L. Nickel cobalt oxide nanowires with iron incorporation realizing a promising electrocatalytic oxygen evolution reaction. *Nanotechnology* **2020**, *31*, 435707. [CrossRef]
54. Anantharaj, S.; Karthik, P.E.; Noda, S. The Significance of Properly Reporting Turnover Frequency in Electrocatalysis Research. *Angew. Chem. Int. Ed.* **2021**, *60*, 23051–23067. [CrossRef]
55. Doyle, R.L.; Godwin, I.J.; Brandon, M.P.; Lyons, M.E.G. Redox and electrochemical water splitting catalytic properties of hydrated metal oxide modified electrodes. *Phys. Chem. Chem. Phys.* **2013**, *15*, 13737–13783. [CrossRef]
56. Binninger, T.; Mohamed, R.; Waltar, K.; Fabbri, E.; Levecque, P.; Kotz, R.; Schmidt, T.J. Thermodynamic explanation of the universal correlation between oxygen evolution activity and corrosion of oxide catalysts. *Sci. Rep.* **2015**, *5*, 12167. [CrossRef]
57. Heli, H.; Yadegari, H. Nanoflakes of the cobaltous oxide, CoO: Synthesis and characterization. *Electrochim. Acta* **2010**, *55*, 2139–2148. [CrossRef]